

Electronic Supporting Information

Syntheses, structural characterization and photophysical properties of two series of rare-earth-isonicotinic-acid containing Waugh-type manganomolybdates

Peijun Gong, Yanyan Li, Cuiping Zhai, Jie Luo, Xuemeng Tian, Lijuan Chen*, and Junwei Zhao*

Henan Key Laboratory of Polyoxometalate Chemistry, Institute of Molecular and Crystal Engineering, College of Chemistry and

Chemical Engineering, Henan University, Kaifeng, Henan 475004, P. R. China

1. Some typical examples of REPOMBMs
2. The structural refinement details in 1–13.
3. Some examples of Mo-containing heterometallic cubane-like clusters, the isometallic cubane {M₄O₄} or heterometallic cubane {M_xM_{4-x}O₄} containing POMs and multi-{M₄O₄} cubane encapsulated POM oligomers
4. IR spectra

Fig. S1 IR spectra of **1–13**.

Fig. S2 a) The Mn-centered triangular {MnMo₃O₁₈} cluster; b) Three triangles ($\Delta 1$, $\Delta 2$, $\Delta 3$) in the [MnMo₉O₃₂]⁶⁻ polyoxoanion.

Fig. S3 a) The 3-D supramolecular packing of **1** viewed along the *a* axis; b) The 3-D supramolecular packing of **1** viewed along the *c* axis.

Fig. S4 (a) The UV spectrum of **3** in the range of 400–200 nm. (b) The UV spectrum of **8** in the range of 400–200 nm. (c) The UV spectral evolution of **3** in the acidic region. (d) The UV spectral evolution of **3** in the alkaline region. (e) The UV spectral evolution of **8** in the acidic region. (f) The UV spectral evolution of **8** in the alkaline region.

Fig. S5 a) The UV spectral evolution of **3** in aqueous solution with time; b) The UV spectral evolution of **8** in aqueous solution with time.

Fig. S6 a) The visible spectrum of (NH₄)₆[MnMo₉O₃₂]·8H₂O in aqueous solution; b) The visible spectrum of **3** in aqueous solution; c) The visible spectrum of **8** in aqueous solution.

Fig. S7 Plots of Kunelka-Munk function versus energy *E* (eV) for **3**, **8** and (NH₄)₆[MnMo₉O₃₂]·8H₂O.

Fig. S8 UV-visible absorption spectral changes for the azophloxine solutions at various irradiation times: a) in the presence of **1** (19.9 mg); b) in the presence of **2** (19.9 mg); c) in the presence of **4** (20.7 mg); d) in the presence of **5** (20.7 mg); e) in the presence of **6** (20.8 mg); f) in the presence of **7** (20.8 mg); g) in the presence of **9** (20.9 mg); h) in the presence of **10** (20.9 mg); i) in the presence of **11** (20.9 mg); j) in the presence of **12** (21 mg); k) in the presence of **13** (20.1 mg); l) in the presence of (NH₄)₆[MnMo₉O₃₂]·8H₂O. Inset: the conversion of azophloxine (γ) with reaction time (*t*). Experimental conditions: the initial concentration of azophloxine: 6 × 10⁻⁵ mol·L⁻¹; the dye solution volume: 50 mL; the catalyst amount: 9.8 × 10⁻⁶ mol (based on [MnMo₉O₃₂]⁶⁻); pH = 2.6.

Fig. S9 UV-visible absorption spectral changes for the azophloxine solutions at various catalyst dosages of **3**: a) 2.46×10⁻⁶ mol (5 mg); b) 9.82×10⁻⁶ mol (20 mg); c) 1.72×10⁻⁵ mol (35 mg); d) 2.46×10⁻⁵ mol (50 mg); e) 3.19×10⁻⁵ mol (65 mg); f) 3.93×10⁻⁵ mol (80 mg); g) 4.66×10⁻⁵ mol (95 mg), and **8**: h) 2.46×10⁻⁶ mol (5.2 mg); i) 9.82×10⁻⁶ mol (20.9 mg); j) 1.72×10⁻⁵ mol (36.6 mg); k) 2.46×10⁻⁵ mol (52.3 mg); l) 3.19×10⁻⁵ mol (67.9 mg); m) 3.93×10⁻⁵ mol (83.6 mg); n) 4.66×10⁻⁵ mol (99.1 mg). Experimental conditions: the initial concentration of azophloxine: 6×10⁻⁵

$^5 \text{ mol} \cdot \text{L}^{-1}$, the dye solution volume: 50 mL, pH = 2.6.

Fig. S10 The effect of the molar ratio of the doped VK-TA18-TiO₂ : **3** on the degradation of azophloxine: a) 0, b) 1:2, c) 1:1, d) 2:1, e) 4:1; The effect of the molar ratio of the doped VK-TA18-TiO₂ : **8** on the degradation of azophloxine: f) 0, g) 1:2, h) 1:1, i) 2:1, j) 4:1. Experimental conditions: the initial concentration of azophloxine: $6 \times 10^{-5} \text{ mol} \cdot \text{L}^{-1}$, the dye solution volume: 50 mL, pH = 2.6.

Fig. S11 Effect of different light intensities and different catalysts on the azophloxine degradation: Under UV light: a) 0.4 mg VK-TA18-TiO₂; b) 20 mg-**3**; c) VK-TA18-TiO₂-TiO₂:**3** (mole ratio) = 1:2 (20 mg **3** and 0.4 mg VK-TA18-TiO₂-TiO₂); d) 20.9 mg-**8**; e) VK-TA18-TiO₂-TiO₂:**8** (mole ratio) = 1:2 (20.9 mg **8** and 0.4 mg VK-TA18-TiO₂-TiO₂). Under visible light: f) 0.4 mg VK-TA18-TiO₂; g) 20 mg-**3**; h) VK-TA18-TiO₂-TiO₂:**3** (mole ratio) = 1:2 (20 mg **3** and 0.4 mg VK-TA18-TiO₂-TiO₂); i) 20.9 mg-**8**; j) VK-TA18-TiO₂-TiO₂:**8** (mole ratio) = 1:2 (20.9 mg **8** and 0.4 mg VK-TA18-TiO₂-TiO₂); k) without any catalyst. Experimental conditions: Initial concentration of azophloxine: $6 \times 10^{-5} \text{ mol} \cdot \text{L}^{-1}$, Volume: 50 mL, pH = 2.6.

Fig. S12 (a) The emission spectrum of (NH₄)₆[MnMo₉O₃₂]·8H₂O under excitation at 340 nm at room temperature; (b) The excitation spectrum of (NH₄)₆[MnMo₉O₃₂]·8H₂O obtained by monitoring the emission at 705 nm; (c) The luminescence decay curve of (NH₄)₆[MnMo₉O₃₂]·8H₂O.

Table S1 Bond valence sum (BVS) parameters for the La1, Mn1, Mo1 and Mo2 in **1**.

Table S2 Summary of RE³⁺ ionic radii, RE–O bond lengths, RE–O Average bond length and RE³⁺ coordination numbers of **1–13**.

1. Some typical examples of REPOMBMs

For instance, in 2002, Das et al. for the first time reported a chain-like extended structure $[\text{La}(\text{H}_2\text{O})_7\text{Al}(\text{OH})_6\text{Mo}_6\text{O}_{18}]_n \cdot 4n\text{H}_2\text{O}$ based on Anderson-type POMB polyanions and lanthanide linkers.¹⁷ Thereafter, Krebs and Wang also communicated Anderson-type REPOMBMs $[(\text{RE}(\text{H}_2\text{O})_6)_2(\text{TeMo}_6\text{O}_{24})] \cdot 10\text{H}_2\text{O}$ ($\text{RE} = \text{Ho}^{3+}, \text{Yb}^{3+}$) and $(\text{C}_6\text{NO}_2\text{H}_5)_2[\text{RE}(\text{H}_2\text{O})_5(\text{CrMo}_6\text{H}_6\text{O}_{24})] \cdot 0.5\text{ H}_2\text{O}$ ($\text{RE} = \text{Ce}^{3+}, \text{La}^{3+}$).¹⁸ In 2003, Wang and co-workers synthesized a series of REPOMBMs consisting of Keggin-type germanomolybdate polyanions $[\text{RE}(\text{NMP})_4(\text{H}_2\text{O})_4][\text{H}_x\text{GeMo}_{12}\text{O}_{40}] \cdot 2\text{ NMP} \cdot 3\text{H}_2\text{O}$ ($\text{RE} = \text{Ce}^{4+}, x = 0; \text{RE} = \text{Pr}^{3+}, \text{Nd}^{3+}, x = 1; \text{NMP} = \text{N-methyl-2-pyrrolidone}$).¹⁹ Soon afterward, Niu's group prepared the RE-supported 1-D polymeric chain phosphomolybdates $[\{\text{RE}(\text{NMP})_6\}(\text{PMo}_{12}\text{O}_{40})]_n$ ($\text{RE} = \text{La}^{3+}, \text{Ce}^{3+}, \text{Pr}^{3+}$).²⁰ In 2012, Chen et al. published two POMB-based RE–pdc metal–organic frameworks $\{[\text{Sm}(\text{H}_2\text{O})_4(\text{pdc})]_3\} \{[\text{Sm}(\text{H}_2\text{O})_3(\text{pdc})]\} [\text{SiMo}_{12}\text{O}_{40}] \cdot 3\text{H}_2\text{O}$ and $\{[\text{La}(\text{H}_2\text{O})_4(\text{pdc})]_4\} [\text{PMo}_{12}\text{O}_{40}]F$ ($\text{H}_2\text{pdc} = \text{pyridine-2,6-dicarboxylic acid}$).²¹

2. The structural refinement details in 1-13

Thanks to the large structures of **1-13** and the existence of a large amount of weight atoms, their intensity data are not very good, leading to the ADP max/min ratio of some atoms, and it is very difficult to refine these large structures, therefore, some unit-occupancy atoms have been refined isotropically and restrainedly refined.

For **1**: O6W-O8W and N6 are refined isotropically. 636 parameters and 1 restraint is used in the refinement.

For **2**: O6W-O8W and N6 are refined isotropically. 637 parameters and 1 restraint is used in the refinement.

For **3**: O6W-O8W and N6 are refined isotropically. 637 parameters and 1 restraint is used in the refinement.

For **4**: O9W, O10W, O13W, O14W, and N5 are refined isotropically. 679 parameters and 2 restraint is used in the refinement.

For **5**: O9W, O10W, O13W, O14W, and N5 are refined isotropically. 679 parameters and 2 restraint is used in the refinement.

For **6**: O9W, O10W, O13W, O14W, and N5 are refined isotropically. 679 parameters and 2 restraint is used in the refinement.

For **7**: O9W, O10W, O13W, O14W, and N5 are refined isotropically. 679 parameters and 2 restraint is used in the refinement.

For **8**: O9W, O10W, O13W, O14W, and N5 are refined isotropically. 679 parameters and 2 restraint is used in the refinement.

For **9**: The "ISOR" instruction is used for C1. O9W, O10W, O13W, O14W, and N5 are refined isotropically. 678 parameters and 8 restraint is used in the refinement.

For **10**: O9W, O10W, O13W, O14W, and N5 are refined isotropically. 679 parameters and 2 restraint is used in the refinement.

For **11**: O9W, O10W, O13W, O14W, and N5 are refined isotropically. 679 parameters and 2 restraint is used in the refinement.

For **12**: O9W, O10W, O13W, O14W, and N5 are refined isotropically. 679 parameters and 2 restraint is used in the refinement.

For **13**: O9W, O10W, O13W, O14W, and N5 are refined isotropically. 678 parameters and 2 restraint is used in the refinement.

3. Some examples of Mo-containing heterometallic cubane-like clusters, the isometallic cubane $\{\text{M}_4\text{O}_4\}$ or heterometallic cubane $\{\text{M}_x\text{M}_{4-x}\text{O}_4\}$ containing POMs and multi- $\{\text{M}_4\text{O}_4\}$ cubane encapsulated POM oligomers

For instance, in 2001, Llusar et al prepared two heterobimetallic cuboidal clusters $[\text{Mo}_3\text{CuS}_4\text{Cl}_4(\text{dmpe})_3](\text{PF}_6)$ and $[\text{Mo}_3\text{CuS}_4\text{Br}_4(\text{dmpe})_3](\text{PF}_6)$ with fine optical-limiting properties by reacting the incomplete cuboidal trimers

[Mo₃S₄Cl₃(dmpe)₃](PF₆) and [Mo₃S₄Br₃(dmpe)₃](PF₆) with CuX (X = Cl⁻, Br⁻) in THF.^{30a} Later, Llusar's group synthesized a pair of enantiomerically pure cuboidal complexes (*P*)-[Mo₃CuS₄{(R,R)-Me-BPE}₃Cl₄]⁺ and (*M*)-[Mo₃CuS₄{(S,S)-Me-BPE}₃Cl₄]⁺.^{30b} In 2009, Zheng and co-workers reported three new heterothiometallic cluster polymers with fascinating topologies [Mo₂O₂S₆Cu₆I₂(4,4'-bipy)₃(H₂O)]_n, [WS₄Cu₄I₂(bpe)₃(H₂O)]_n and [WS₄Cu₆I₄(timtz)_{8/3}(H₂O)₁₂]_n.³¹ In addition, the isometallic cubane {M₄O₄} or heterometallic cubane {M_xM_{4-x}O₄} containing POMs have been previously found.³² For instance, in 1999, Kortz et al communicated an interesting ferromagnetic mono-{Ni₄O₄}-cubane-capped Keggin phosphotungstate [H₂PW₉Ni₄O₃₄(OH)₃(H₂O)₆]²⁻.^{32a} In the same year, Coronado's group discovered a ferromagnetic mono-{Ni₃WO₄}-cubane substituted Keggin phosphotungstate species [Ni₃(H₂O)₃(PW₁₀O₃₉)H₂O]⁷⁻.^{32b} In 2009, three 3d-4f heterometallic cubane {RECu₃(OH)₃O} (RE = La³⁺, Gd³⁺, Eu³⁺) inserted Keggin silicotungstates were obtained by Mialane and co-workers.^{32c} In 2010, Fang et al reported a mixed-valence cubane {Mn^{III}₃Mn^{IV}O₄} embedded Dawson phosphotungstate [(α -P₂W₁₅O₅₆)Mn^{III}₃Mn^{IV}O₃(CH₃COO)₃]⁸⁻ that exhibits a single-molecule magnet behavior.^{32d} Furthermore, multi-{M₄O₄} cubane encapsulated POM oligomers were also made. In 2007, Yang et al communicated a mixed-valence tetrameric phosphotungstate aggregate [{Fe^{II}_{1.5}Fe^{III}₁₂(μ_3 -OH)₁₂(μ_4 -PO₄)₄(B- α -PW₉O₃₄)₄]²⁰⁻ containing one {Fe^{II}O₄} and four {Fe^{III}₃Fe^{II}O(OH)₃} cubane units, which illustrates the antiferromagnetic coupling interactions within magnetic centers.^{32e} Later, multi-{Ni₄O₄}, multi-{Mn₄O₄} and multi-{Co₄O₄} cubane-unit encapsulated POMs were consecutively found by Wang's group.^{32f-h}

4. IR spectra

IR spectra of **1–13** have been investigated between 4000 and 400 cm⁻¹ on a Nicolet 170 SXFT-IR spectrometer by utilizing KBr pellets (Fig. S1 in ESI). Their IR spectra show similar characteristic peaks for the skeletal vibrations in the region between 400 and 1000 cm⁻¹, indicating that **1–13** contain the same polyoxoanion skeleton, which is in good agreement with the results of single-crystal X-ray diffraction analysis. In **1–3**, the intense absorption bands at 941–939 cm⁻¹ and 901–900 cm⁻¹ correspond to the v(Mo–O_t) stretching vibration, those at 681–680 cm⁻¹ and 595–593 cm⁻¹ are assigned to the v(Mo–O_b–Mo) stretching vibration and the absorption band appearing at 543–542 cm⁻¹ is attributed to the Mn–O stretching vibration.^{1,2} Correspondingly, these characteristic peaks are observed at 936–933 cm⁻¹ and 905–900 cm⁻¹; 685–682 cm⁻¹, 595–593 cm⁻¹; and 543–540 cm⁻¹ in **4–13**. Furthermore, the v(Mo–O_t) absorption vibration bands of **1–13** show the bathochromic shift red-shifts in comparison with the v(Mo–O_t) absorption vibration band (927, 881 cm⁻¹) of K_{1.5}(NH₄)_{4.5}[MnMo₉O₃₂]·4.2H₂O,^{2b} the probable reason for which may be that there are comparatively stronger interactions between the {[RE(Hina)(ina)(H₂O)₂]₂]⁴⁺ or [RE(Hina)₂(H₂O)₆]³⁺ cations and the terminal oxygen atoms of the [MnMo₉O₃₂]⁶⁻ polyoxoanions, whittling the Mo–O_t bonds, reducing the Mo–O_t bond force constant, and leading to the diminishing in the Mo–O_t vibration frequency.³ In addition, the strong broad band at around 3400 cm⁻¹ is assigned to the stretching vibration mode of coordinate and lattice water molecules. As a rule, the carboxylic group is anticipated to show very intense absorption bands from asymmetric (1500–1630 cm⁻¹) and symmetric (1350–1460 cm⁻¹) stretching vibration.^{4a,b} Apparently, the absorption bands observed at 1642–1637 cm⁻¹, 1592–1590 cm⁻¹ and 1404–1402 cm⁻¹ for **1–3** and 1613–1608 cm⁻¹ and 1397–1393 cm⁻¹ for **4–13** are attributed to the asymmetric [v_{as}(CO₂⁻)] and symmetric [v_{sy}(CO₂⁻)] stretching vibrations of carboxylic groups of the ina ligands, respectively.^{4b,c} In general, the separation ($\Delta\nu$) between v_{as}(CO₂⁻) and v_{sy}(CO₂⁻) in the IR spectrum has been effectively used to obtain information concerning bonding modes of carboxylic groups.^{4a-c} If $\Delta\nu$ is larger than 200 cm⁻¹, the carboxylic group employs the monodentate coordination mode, in contrast, if $\Delta\nu$ is smaller than 200 cm⁻¹, the carboxylic group utilizes the chelating coordination pattern.^{4d} Therefore, the occurrence of $\Delta\nu$ of 240–233 cm⁻¹ and 190–186 cm⁻¹ for **1–3** illustrates the coexistence of monodentate and chelating coordination modes of the carboxylic groups in **1–3** while $\Delta\nu$ of 220–211 cm⁻¹ for **4–13** indicates the monodentate coordination mode of the carboxylic groups in **4–13**. These results are consistent with their crystal structures. The signal appearing at 3164–3153 cm⁻¹ for **1–13** is attributable to the v(N–H) stretching vibration of NH₄⁺.² In a word, the results of IR spectra coincide with those

from the X-ray single-crystal structural analysis.

- 1 L. O. Gavrilova and V. N. Molchanov. *Russ. J. Coord. Chem.*, 2005, **31**, 401.
- 2 (a) S. Lin, Y. Zhen, S. M. Wang and Y. M. Dai, *J. Mol. Catal. A: Chem.*, 2000, **156**, 113; (b) D. Zammel, I. Nagazi and A. Haddad, *J. Clust. Sci.*, 2015, **26**, 1693.
- 3 (a) J. P. Wang, X. Y. Duan, X. D. Du and J. Y. Niu, *Cryst. Growth Des.*, 2006, **6**, 2266; (b) J. P. Wang, J. W. Zhao, X. Y. Duan and J. Y. Niu, *Cryst. Growth Des.*, 2006, **6**, 507.
- 4 (a) K. C. Szeto, K.P. Lillerud, M. Tilset, M. Bjørgen, C. Prestipino, A. Zecchina, C. Amberti and S. Bordiga, *J. Phys. Chem. B*, 2006, **110**, 21509; (b) S. Bordiga, C. Lamberti, G. Ricchiardi, L. Regli, F. Bonino, A. Damin, K. P. Lillerud, M. Bjørgen and A. Zecchina, *Chem. Commun.*, 2004, 2300; (c) V. F. Zolin, L. N. Puntus, V. I. Tsaryuk, V. A. Kudryashova, J. Legendziewicz, P. Gawryszecka and R. Szostak, *J. Alloys. Compd.*, 2004, **380**, 279.
- 5 (a) V. Tsaryuk, I. Turowska-Tyrk, J. Legendziewicz, V. Zolin, R. Szostak and L. Puntus, *J. Alloys. Compd.*, 2002, **341**, 323; (b) V. F. Zolin, L. N. Puntus, V. I. Tsaryuk, V. A. Kudryashova, J. Legendziewicz, P. Gawryszecka and R. Szostak, *J. Alloys. Compd.*, 2004, **380**, 279; (c) C. H. Li, K. L. Huang, Y. N. Chi, X. Liu, Z. G. Han, L. Shen and C. W. Hu, *Inorg. Chem.*, 2009, **48**, 2010; (d) K. Nakamoto, *Infrared and Raman Spectra of Inorganic and Coordination Compounds*, 3rd Ed.; New York: John Wiley and Sons, 1978.

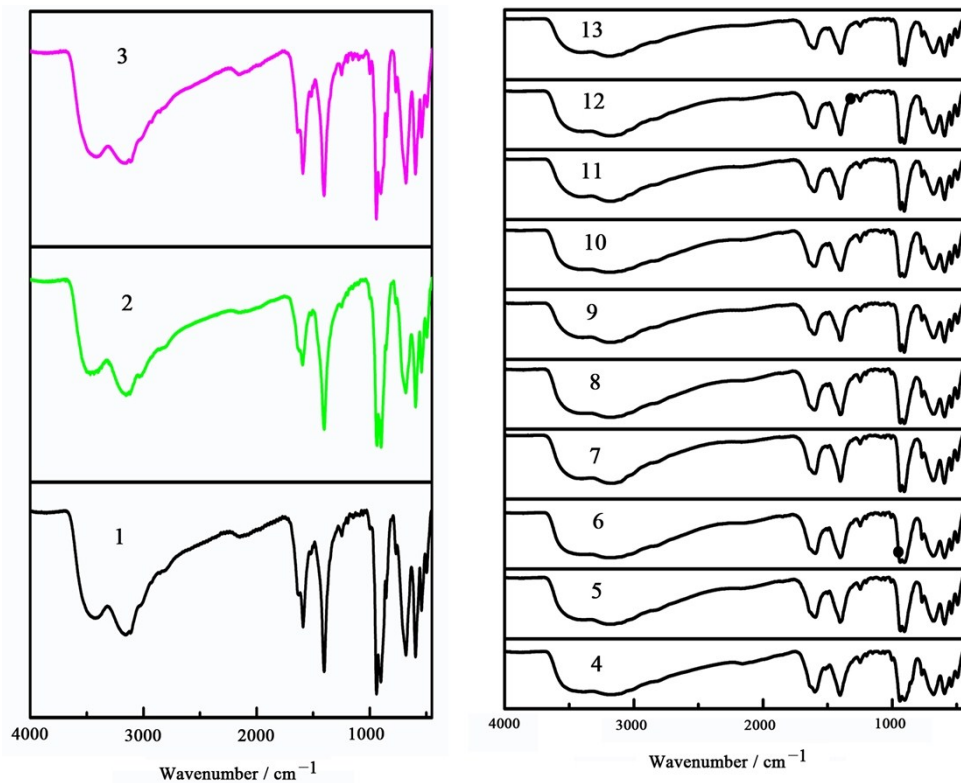


Fig. S1 IR spectra of 1–13.

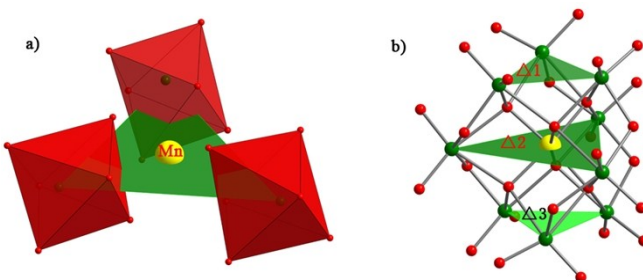


Fig. S2 a) The Mn-centered triangular $\{\text{MnMo}_3\text{O}_{18}\}$ cluster; b) Three triangles (Δ_1 , Δ_2 , Δ_3) in the $[\text{MnMo}_9\text{O}_{32}]^{6-}$ polyoxoanion.

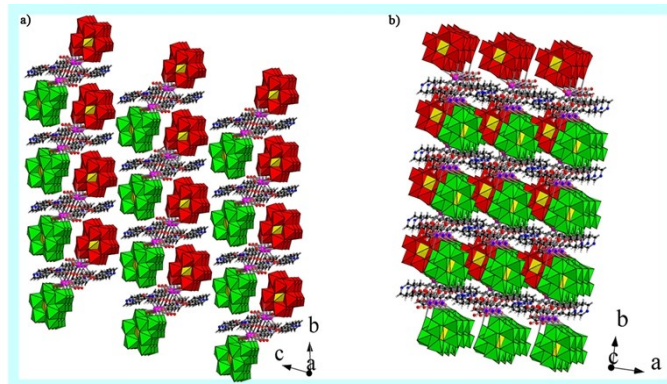


Fig. S3 a) The 3-D supramolecular packing of **1** viewed along the *a* axis; b) The 3-D supramolecular packing of **1** viewed along the *c* axis.

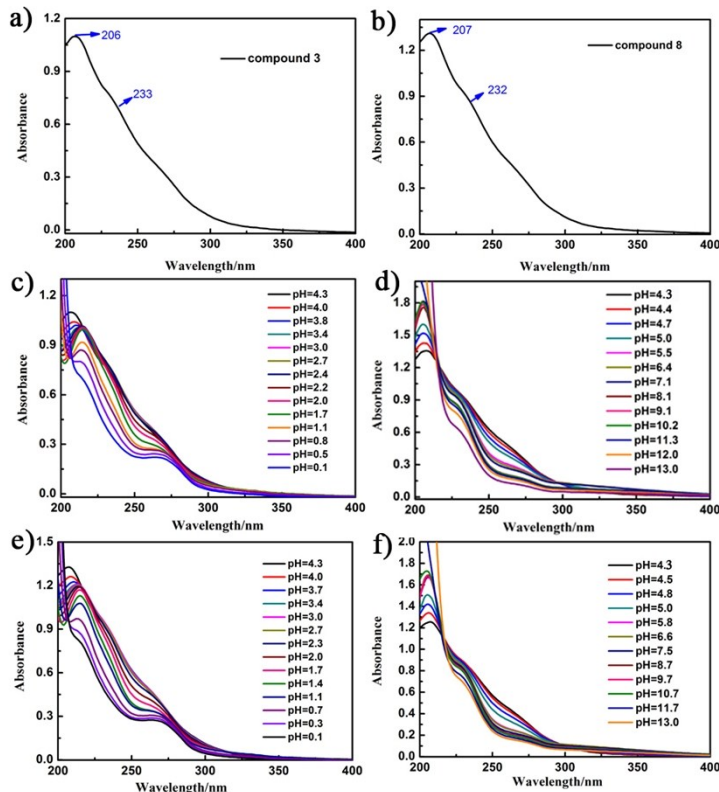


Fig. S4 (a) The UV spectrum of **3** in the range of 400–200 nm. (b) The UV spectrum of **8** in the range 400–200 nm. (c) The UV spectral evolution of **3** in the acidic region. (d) The UV spectral evolution of **3** in the alkaline region. (e) The UV spectral evolution of **8** in the acidic region. (f) The UV spectral evolution of **8** in the alkaline region.

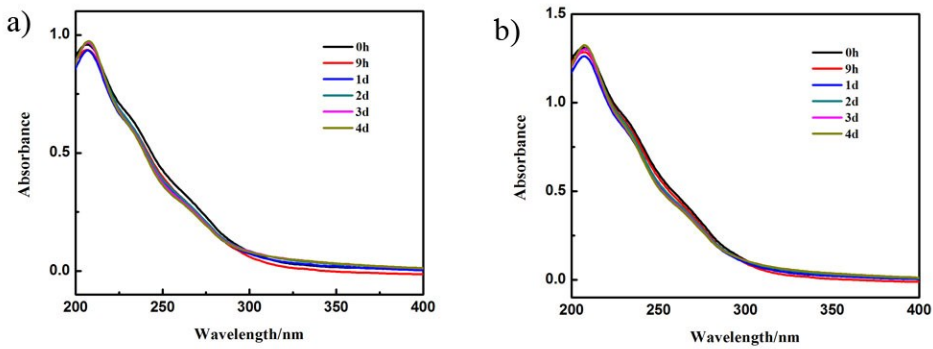


Fig. S5 a) The UV spectral evolution of **3** in aqueous solution with time; b) The UV spectral evolution of **8** in aqueous solution with time.

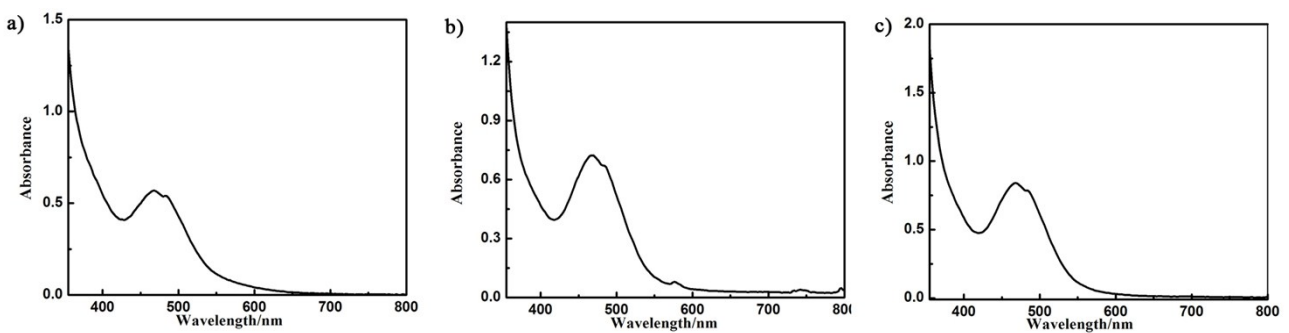


Fig. S6 a) The visible spectrum of $(\text{NH}_4)_6[\text{MnMo}_9\text{O}_{32}]\cdot 8\text{H}_2\text{O}$ in aqueous solution; b) The visible spectrum of **3** in aqueous solution; c) The visible spectrum of **8** in aqueous solution.

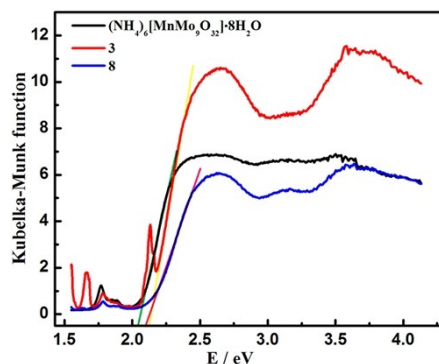


Fig. S7 Plots of Kubelka-Munk function versus energy E (eV) for **3**, **8** and $(\text{NH}_4)_6[\text{MnMo}_9\text{O}_{32}]\cdot 8\text{H}_2\text{O}$.

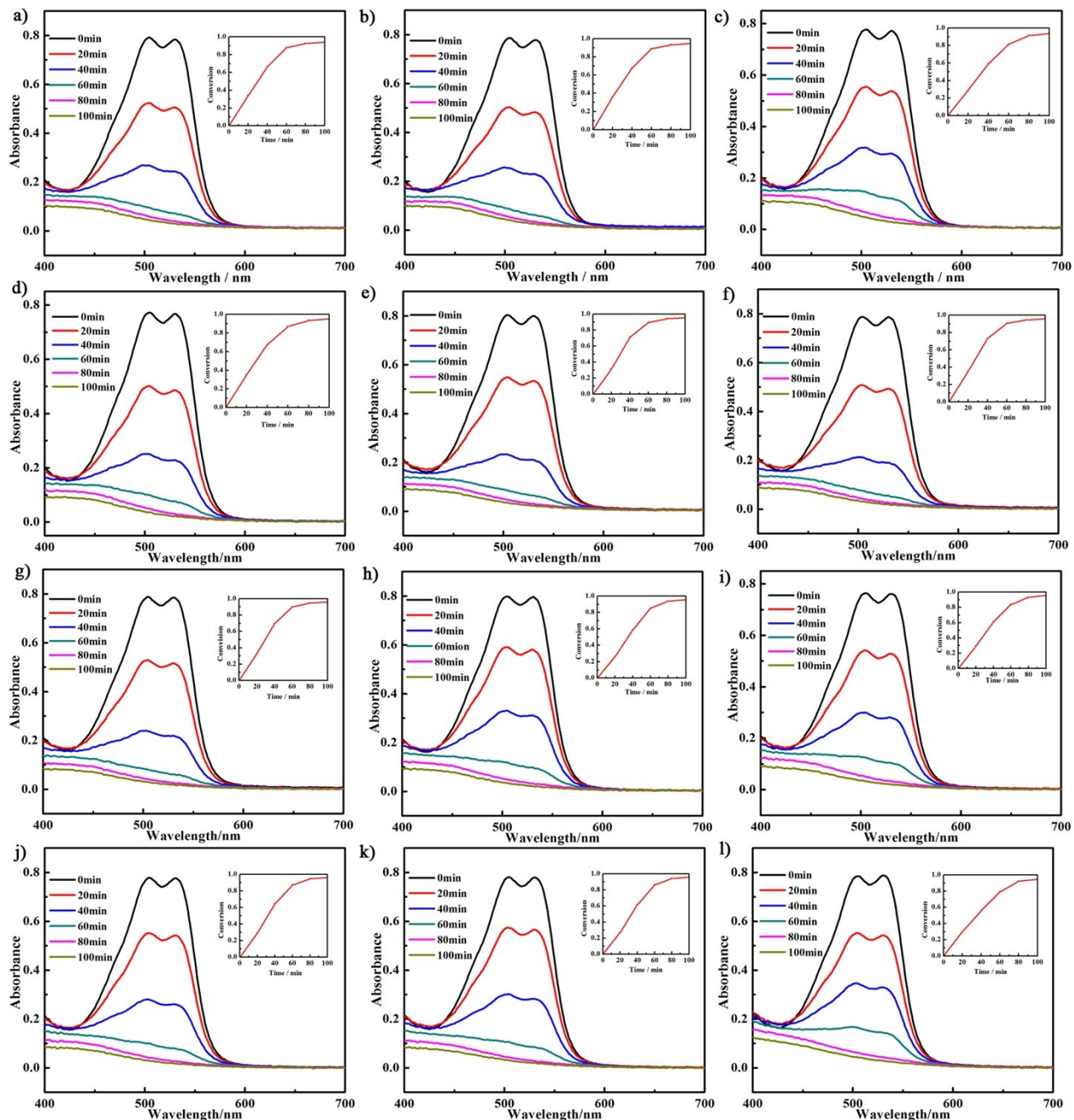


Fig. S8 UV-visible absorption spectral changes for the azophloxine solutions at various irradiation times: a) in the presence of **1** (19.9 mg); b) in the presence of **2** (19.9 mg); c) in the presence of **4** (20.7 mg); d) in the presence of **5** (20.7 mg); e) in the presence of **6** (20.8 mg); f) in the presence of **7** (20.8 mg); g) in the presence of **9** (20.9 mg); h) in the presence of **10** (20.9 mg); i) in the presence of **11** (20.9 mg); j) in the presence of **12** (21 mg); k) in the presence of **13** (20.1 mg); l) in the presence of $(\text{NH}_4)_6[\text{MnMo}_9\text{O}_{32}] \cdot 8\text{H}_2\text{O}$. Inset: the conversion of azophloxine (y) with reaction time (t). Experimental conditions: the initial concentration of azophloxine: $6 \times 10^{-5} \text{ mol} \cdot \text{L}^{-1}$; the dye solution volume: 50 mL; the catalyst amount: $9.8 \times 10^{-6} \text{ mol}$ (based on $[\text{MnMo}_9\text{O}_{32}]^{6-}$); pH = 2.6.

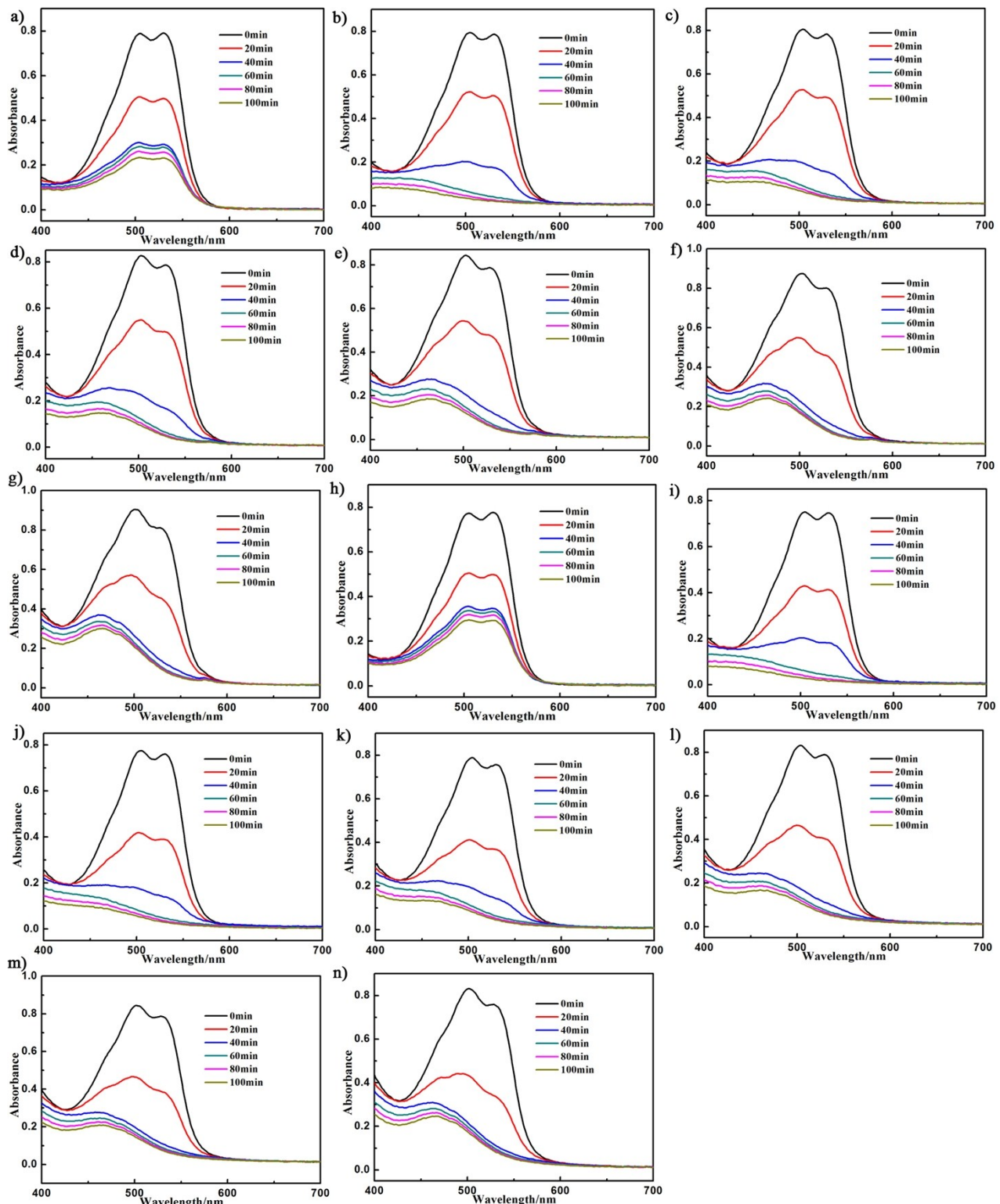


Fig. S9 UV-visible absorption spectral changes for the azophloxine solutions at various catalyst dosages of **3**: a) 2.46×10^{-6} mol (5 mg); b) 9.82×10^{-6} mol (20 mg); c) 1.72×10^{-5} mol (35 mg); d) 2.46×10^{-5} mol (50 mg); e) 3.19×10^{-5} mol (65 mg); f) 3.93×10^{-5} mol (80 mg); g) 4.66×10^{-5} mol (95 mg), and **8**: h) 2.46×10^{-6} mol (5.2 mg); i) 9.82×10^{-6} mol (20.9 mg); j) 1.72×10^{-5} mol (36.6 mg); k) 2.46×10^{-5} mol (52.3 mg); l) 3.19×10^{-5} mol (67.9 mg); m) 3.93×10^{-5} mol (83.6 mg); n) 4.66×10^{-5} mol (99.1 mg). Experimental conditions: the initial concentration of azophloxine: 6×10^{-5} mol·L⁻¹, the dye solution volume: 50 mL, pH = 2.6.

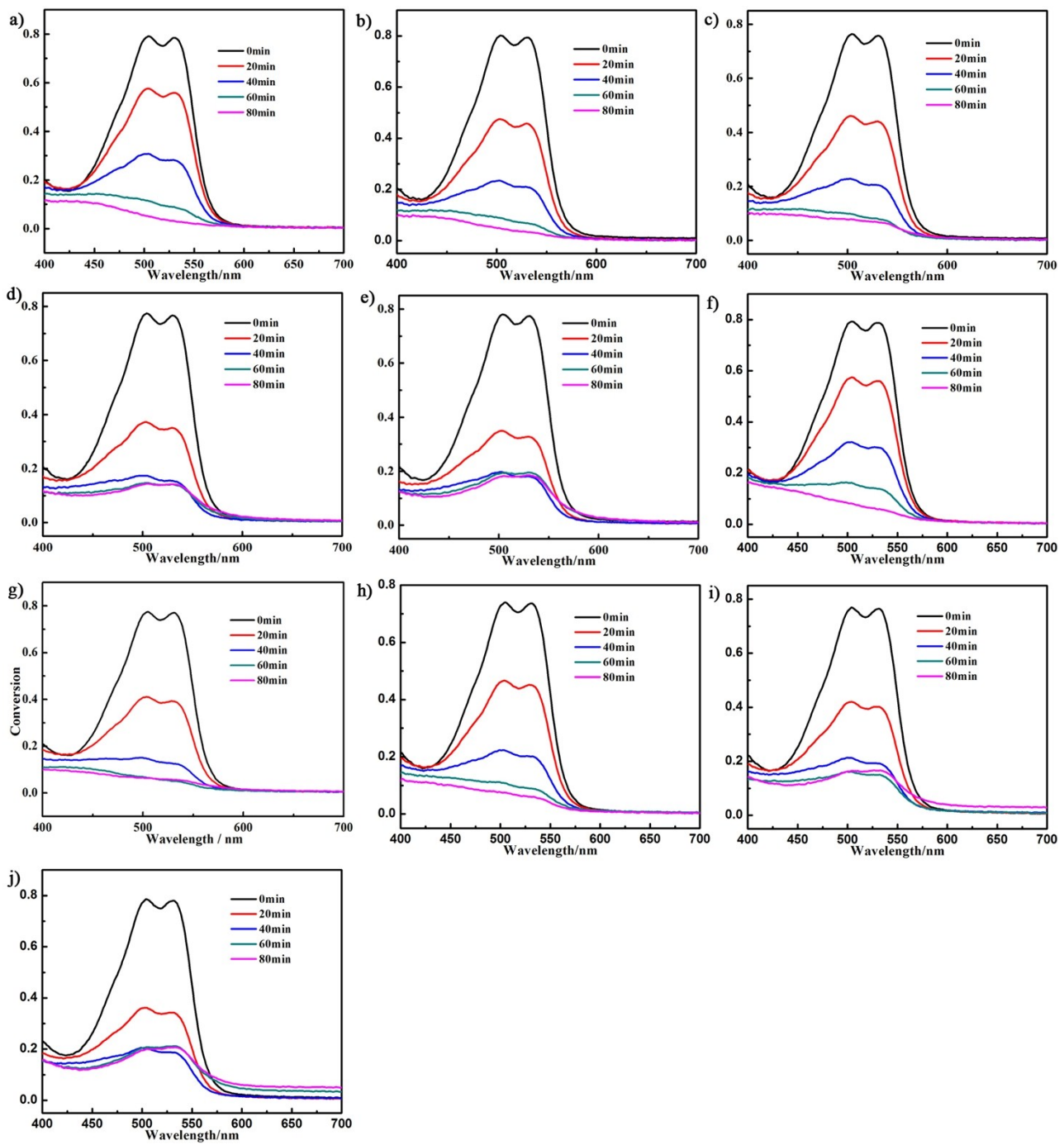


Fig. S10 The effect of the molar ratio of the doped VK-TA18-TiO₂ : **3** on the degradation of azophloxine: a) 0, b) 1:2, c) 1:1, d) 2:1, e) 4:1; The effect of the molar ratio of the doped VK-TA18-TiO₂ : **8** on the degradation of azophloxine: f) 0, g) 1:2, h) 1:1, i) 2:1, j) 4:1. Experimental conditions: the initial concentration of azophloxine: 6×10^{-5} mol·L⁻¹, the dye solution volume: 50 mL, pH = 2.6.

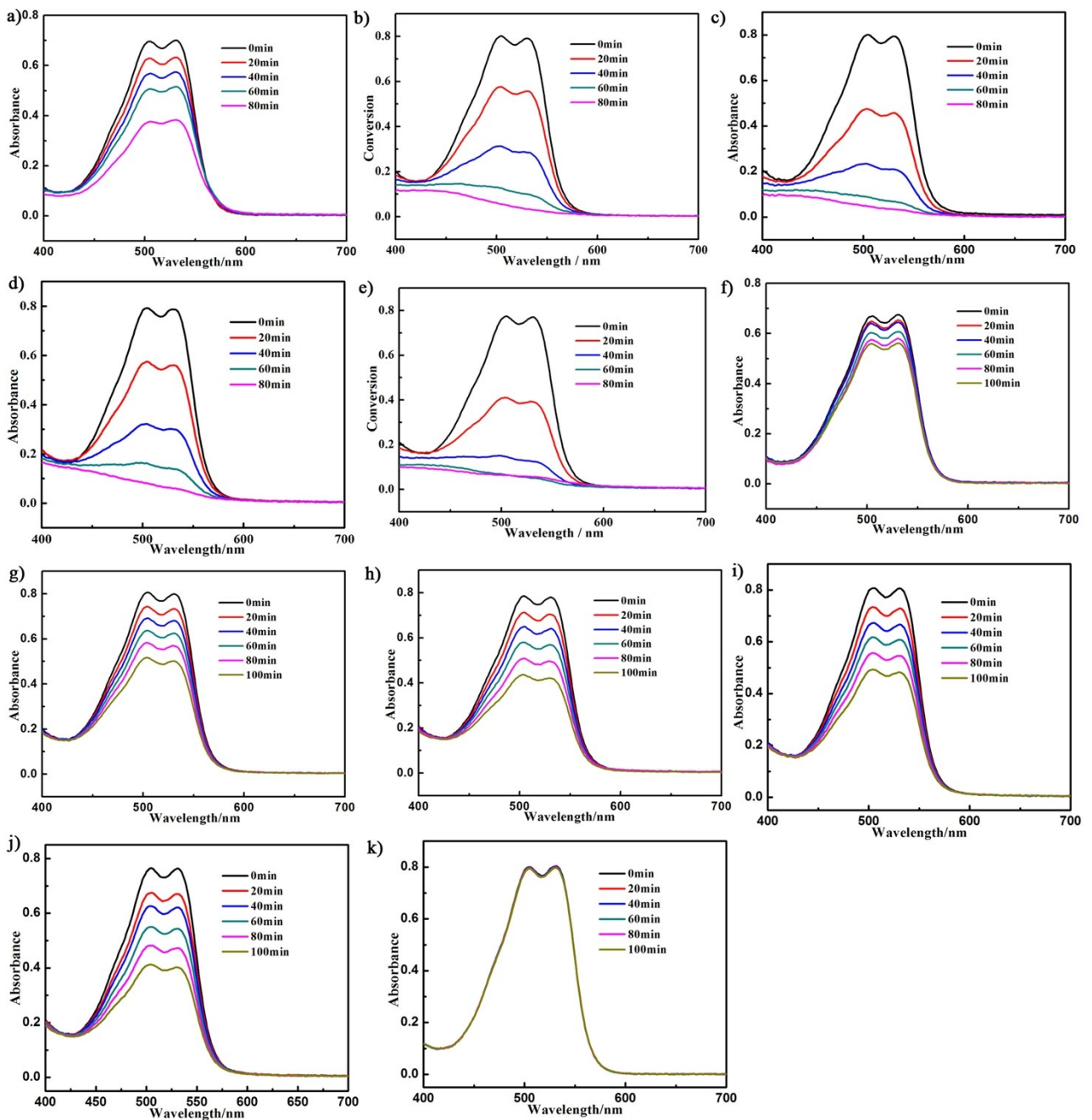


Fig. S11 Effect of different light intensities and different catalysts on the azophloxine degradation: Under UV light: a) 0.4 mg VK-TA18-TiO₂; b) 20 mg-3; c) VK-TA18-TiO₂-TiO₂:3 (mole ratio) = 1:2 (20 mg 3 and 0.4 mg VK-TA18-TiO₂-TiO₂); d) 20.9 mg-8; e) VK-TA18-TiO₂-TiO₂:8 (mole ratio) = 1:2 (20.9 mg 8 and 0.4 mg VK-TA18-TiO₂-TiO₂). Under visible light: f) 0.4 mg VK-TA18-TiO₂; g) 20 mg-3; h) VK-TA18-TiO₂-TiO₂:3 (mole ratio) = 1:2 (20 mg 3 and 0.4 mg VK-TA18-TiO₂-TiO₂); i) 20.9 mg-8; j) VK-TA18-TiO₂-TiO₂:8 (mole ratio) = 1:2 (20.9 mg 8 and 0.4 mg VK-TA18-TiO₂-TiO₂); k) without any catalyst. Experimental conditions: Initial concentration of azophloxine: 6×10^{-5} mol·L⁻¹, Volume: 50 mL, pH = 2.6.

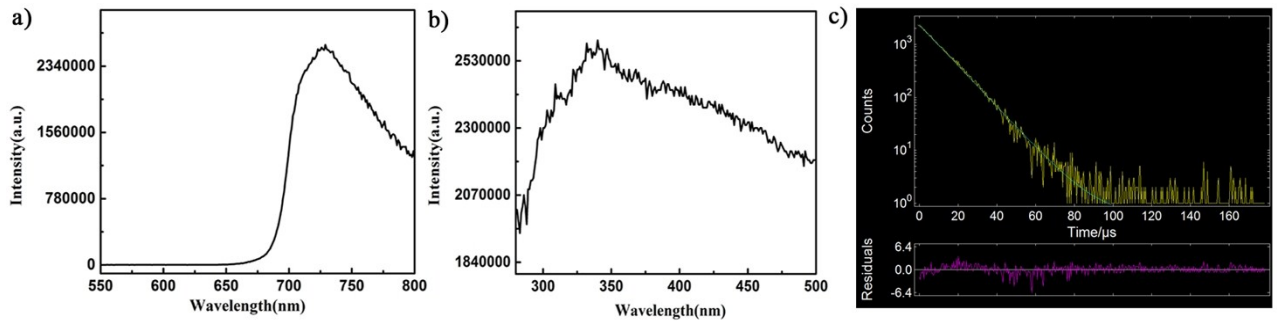


Fig. S12 (a) The emission spectrum of $(\text{NH}_4)_6[\text{MnMo}_9\text{O}_{32}] \cdot 8\text{H}_2\text{O}$ under excitation at 340 nm at room temperature; (b) The excitation spectrum of $(\text{NH}_4)_6[\text{MnMo}_9\text{O}_{32}] \cdot 8\text{H}_2\text{O}$ obtained by monitoring the emission at 705 nm; (c) The luminescence decay curve of $(\text{NH}_4)_6[\text{MnMo}_9\text{O}_{32}] \cdot 8\text{H}_2\text{O}$.

Table S1 Bond valence sum (BVS) parameters for the La1, Mn1, Mo1 and Mo2 in **1**.

Bond	Bond length	Bond valence	Bond valence sum
La1–O34	2.491(8)	0.42	$\sum(\text{La1}) = 2.95$
La1–O36	2.495(7)	0.42	
La1–O23	2.517(6)	0.39	
La1–O35#1	2.540(7)	0.37	
La1–O26	2.541(6)	0.37	
La1–O2W	2.553(8)	0.36	
La1–O1W	2.592(9)	0.32	
La1–O19	2.614(6)	0.30	
Mn1–O21	1.872(6)	0.73	$\sum(\text{Mn1}) = 4.18$
Mn1–O5	1.887(6)	0.70	
Mn1–O28	1.890(6)	0.69	
Mn1–O14	1.891(6)	0.69	
Mn1–O10	1.891(6)	0.69	
Mn1–O4	1.896(6)	0.68	
Mo1–O1	1.688(7)	1.81	$\sum(\text{Mo1}) = 6.06$
Mo1–O2	1.694(7)	1.78	
Mo1–O6	1.964(7)	0.86	
Mo1–O3	1.965(7)	0.86	
Mo1–O4	2.250(6)	0.40	
Mo1–O5	2.291(6)	0.35	$\sum(\text{Mo2}) = 5.98$
Mo2–O7	1.704(6)	1.73	
Mo2–O8	1.712(7)	1.69	
Mo2–O6	1.874(6)	1.09	
Mo2–O9	2.074(6)	0.64	
Mo2–O5	2.204(6)	0.45	
Mo2–O10	2.263(6)	0.38	

Table S2 Summary of RE³⁺ ionic radii, RE–O bond lengths, RE–O Average bond length and RE³⁺ coordination numbers of **1–13**.

Compound	RE ³⁺	RE ³⁺ ionic radii (Å)	RE–O bond lengths (Å)	RE–O average bond lengths (Å)	RE ³⁺ coordination number
1	La ³⁺	1.061	La(1)–O(34) 2.491(8) La(1)–O(36) 2.495(7) La(1)–O(23) 2.517(6) La(1)–O(35)#1 2.540(7) La(1)–O(26) 2.541(6) La(1)–O(2W) 2.553(8) La(1)–O(1W) 2.592(9) La(1)–O(19) 2.614(6) La(1)–O(35) 2.963(7)	2.590	9
2	Pr ³⁺	1.013	Pr(1)–O(34) 2.425(5) Pr(1)–O(36) 2.465(4) Pr(1)–O(1W) 2.465(5) Pr(1)–O(35)#1 2.473(4) Pr(1)–O(26) 2.483(4) Pr(1)–O(23) 2.485(4) Pr(1)–O(2W) 2.516(4) Pr(1)–O(19) 2.574(4) Pr(1)–O(35) 3.045(4)	2.548	9
3	Nd ³⁺	0.995	Nd(1)–O(34) 2.416(5) Nd(1)–O(35)#1 2.444(5) Nd(1)–O(36) 2.447(5) Nd(1)–O(1W) 2.459(6) Nd(1)–O(26) 2.465(5) Nd(1)–O(23) 2.472(5) Nd(1)–O(2W) 2.505(5) Nd(1)–O(19) 2.556(5) Nd(1)–O(35) 3.081(4)	2.538	9
4	Sm ³⁺	0.964	Sm(1)–O(33) 2.319(4) Sm(1)–O(35) 2.364(3) Sm(1)–O(6W) 2.406(3) Sm(1)–O(1W) 2.428(4) Sm(1)–O(2W) 2.446(4) Sm(1)–O(4W) 2.453(3) Sm(1)–O(3W) 2.471(4) Sm(1)–O(5W) 2.483(4)	2.421	8
5	Eu ³⁺	0.950	Eu(1)–O(33) 2.300(5) Eu(1)–O(35) 2.349(4) Eu(1)–O(6W) 2.392(4) Eu(1)–O(1W) 2.407(5)	2.403	8

			Eu(1)–O(2W)	2.433(5)		
			Eu(1)–O(4W)	2.435(4)		
			Eu(1)–O(3W)	2.449(6)		
			Eu(1)–O(5W)	2.462(5)		
6	Gd ³⁺	0.938	Gd(1)–O(33)	2.303(5)	2.399	8
			Gd(1)–O(35)	2.344(4)		
			Gd(1)–O(6W)	2.383(4)		
			Gd(1)–O(1W)	2.412(5)		
			Gd(1)–O(4W)	2.426(4)		
			Gd(1)–O(2W)	2.428(5)		
			Gd(1)–O(3W)	2.440(5)		
			Gd(1)–O(5W)	2.454(5)		
7	Tb ³⁺	0.923	Tb(1)–O(33)	2.277(5)	2.381	8
			Tb(1)–O(35)	2.322(4)		
			Tb(1)–O(6W)	2.375(4)		
			Tb(1)–O(1W)	2.386(5)		
			Tb(1)–O(2W)	2.409(4)		
			Tb(1)–O(4W)	2.413(4)		
			Tb(1)–O(3W)	2.430(5)		
			Tb(1)–O(5W)	2.434(4)		
8	Dy ³⁺	0.908	Dy1–O(33)	2.273(6)	2.369	8
			Dy1–O(35)	2.310(5)		
			Dy1–O(6W)	2.351(5)		
			Dy1–O(1W)	2.382(6)		
			Dy1–O(4W)	2.397(5)		
			Dy1–O(2W)	2.398(5)		
			Dy1–O(3W)	2.415(6)		
			Dy1–O(5W)	2.422(5)		
9	Ho ³⁺	0.894	Ho(1)–O(33)	2.259(7)	2.361	8
			Ho(1)–O(35)	2.306(6)		
			Ho(1)–O(6W)	2.351(6)		
			Ho(1)–O(1W)	2.377(7)		
			Ho(1)–O(2W)	2.391(6)		
			Ho(1)–O(4W)	2.394(6)		
			Ho(1)–O(3W)	2.402(7)		
			Ho(1)–O(5W)	2.408(6)		
10	Er ³⁺	0.881	Er(1)–O(33)	2.267(6)	2.367	8
			Er(1)–O(35)	2.320(5)		
			Er(1)–O(6W)	2.347(6)		
			Er(1)–O(1W)	2.384(6)		
			Er(1)–O(4W)	2.398(5)		
			Er(1)–O(2W)	2.401(6)		
			Er(1)–O(5W)	2.406(6)		
			Er(1)–O(3W)	2.410(7)		

11	Tm ³⁺	0.870	Tm(1)–O(33) Tm(1)–O(35) Tm(1)–O(6W) Tm(1)–O(1W) Tm(1)–O(2W) Tm(1)–O(4W) Tm(1)–O(3W) Tm(1)–O(5W)	2.267(5) 2.315(4) 2.347(4) 2.378(5) 2.390(5) 2.394(4) 2.398(5) 2.412(4)	2.363	8
12	Yb ³⁺	0.858	Yb(1)–O(33) Yb(1)–O(35) Yb(1)–O(6W) Yb(1)–O(1W) Yb(1)–O(3W) Yb(1)–O(4W) Yb(1)–O(2W) Yb(1)–O(5W)	2.226(5) 2.285(4) 2.316(5) 2.344(5) 2.354(6) 2.359(4) 2.360(5) 2.374(5)	2.327	8
13	Y ³⁺	0.893	Y(1)–O(33) Y(1)–O(35) Y(1)–O(6W) Y(1)–O(1W) Y(1)–O(3W) Y(1)–O(2W) Y(1)–O(4W) Y(1)–O(5W)	2.261(5) 2.315(4) 2.340(4) 2.384(5) 2.385(5) 2.387(4) 2.395(4) 2.409(4)	2.360	8